Development and Validation of a Methodology for Numerical Calibration of Five-Hole Probes

Konstantin Speck, Alexander Rabl, Christian Helcig, Volker Gümmer
Technical University of Munich
TUM School of Engineering and Design
Institute of Turbomachinery and Flight Propulsion
85748 Garching bei München
konstantin.speck@tum.de

Abstract

Understanding flow phenomena in turbomachinery poses an ongoing challenge, demanding precise characterization of the flow field in the respective domain. Pneumatic multi-hole probes are an important tool for such measurements, quantifying flow parameters such as pressures, angles, and Mach numbers. To support the designer of state-of-the-art turbomachinery, it is necessary to reduce the measurement uncertainties associated with the usage of these types of probes in real operating conditions.
Numerical investigations can be used to investigate probe behavior under flow conditions that are experimentally unattainable during calibration. Building upon a previous paper, a numerical model incorporating real geometries is developed for numerical calibration. Five approaches of modeling spherical five-hole probe geometries are compared, including a real geometry scan with a resolution of 0.005 mm generated with a Micro CT. Meshes of these geometries are generated using Ansys Fluent Meshing. The flow field around the probe head and inside the probe holes is resolved using Fluent 2024.R1. From the resulting probe hole pressures, calibration coefficients are calculated and compared to experimental data.
For well-resolved geometries, numerically generated calibration data exhibit similar quality compared to experimental data. A flow field analysis provides insights into the complex vortex structures and their behavior inside the probe holes, emphasizing their impact on pressure measurements.
The developed methodology can enhance the understanding of measurement uncertainties in turbomachinery and can potentially extend calibration maps into new dimensions.

Keywords: Pressure probes, Five-Hole probe, Real geometry, Numerical calibration

NOMENCLATURE

5HP	Five-hole probe
BC	Boundary condition
CAD	Computer aided design
CFD	Computational fluid dynamics
CT	Computed tomography
GCI	Grid convergence index
GEKO	Generalized k-ω turbulence model
SAPS	Shop air pressure system
HSRC	High speed research compressor
LTF	Institute of Turbomachinery and Flight Propulsion
PH	Probe hole
PHd	Probe head
R	Rotor of a compressor stage
RANS	Reynolds averaged Navier Stokes
RTD	Resistance temperature detector
SST	Shear stress transport turbulence model
scan	Real geometry 3D scan
scan smooth	Real geometry 3D scan with smoothed surface
TUM	Technical University Munich
URANS	Unstedy Reynolds averaged Navier Stokes
w PH	With probe holes
w PH pos	With probe holes positioned
wo PH	Without probe holes

Greek Symbols

α	Yaw angle in [°]
β	Pitch angle in [°]
Φ	Variable for GCI

1 INTRODUCTION

To precisely characterize flow in modern high-speed compressors and turbines, detailed, spatially highly-resolved measurements with pneumatic multi-hole probes are essential. Such probes are commonly used to quantify flow parameters like pressure, angles, and Mach numbers. Typically, these probes undergo meticulous calibration in specialized wind tunnel settings with stable, low-turbulence conditions at ambient pressure, covering various Mach numbers. However, in real high-speed turbomachinery applications, these probes can encounter different conditions compared to the calibration. Velocity gradients [1], high turbulence [2], changes in Reynolds number [3], unsteadiness [4], and aging of the probe considerably change the aerodynamic performance of the probe, adding errors to the measurement. Some of these phenomena have been investigated, and some corrections are available, but not all measurement errors are well understood.
Computational Fluid Dynamics (CFD) can help to better understand and quantify the occurring errors. Furthermore, a good and reliable CFD model for investigations of the flow around a pressure probe head (PHd) can potentially support or replace expensive experimental calibration. Flow conditions, similar to the working conditions of the probe, can be easily defined in CFD. For instance, for each individual probe geometry, the Reynolds number can be varied using a numerical approach, while experiments require an expensive and complex pressure chamber.

The first numerical investigations on pressure probes date back to De Guzman et al. 1994 [5]. De Guzman focused on separation at different flow angles at the tip of a pyramid probe. While the total pressure shows only a small discrepancy with respekct to to experimental data for small flow angles, the side hole pressures tend to deviate strongly.

Coldrick et al. [6] conducted a thorough numerical investigation into the measurement uncertainties of five-hole probes (5HP) in compressor flows using both steady and unsteady flow simulations. To accomplish this, a numerical calibration map to analyze the blockage effects of multi-hole probes in compressor applications was created. A key observation was that disruptions in a steady state could lead to errors in the probe measurements. At the same time, the influence of the unsteadiness generated by a compressor had a minimal impact on the probe characteristics. Using the numerical calibration, the total pressure coefficient was underestimated by approx 30 % while the yaw coefficient showed a different behavior for varying yaw angles.
In an investigation by Aschenbruck et al. [7], good agreement for total pressure and pitch angle coefficients was shown, while the yaw angle coefficient shows a constant offset, likely caused by misalignment. Further, the static pressure coefficient presented an offset, and a different behavior with flow angle variation.
Sanders et al. [8] calibrated a spherical probe over a wide range of Mach numbers (0.1 to 0.9) and flow angles, leading to 1089 simulations. While obtaining only minor differences in the calibration map, Sanders et al. [8] state that the numerical calibration should not be used to replace the experimental calibration. Nonetheless, it can be used in numerical simulations to process the pressure acquired by a numerical probe.
The first study taking the real-geometry of the probe head into account was conducted by Passmann et al. [9]. A 3D-printed conical 5HP was scanned, and a CAD model was built following the information gained from the real geometry scan. The probe holes of the scan are projected on the conical surface of the ideal geometry, but the probe holes are not included in the model.
Schäffer et al. [10] compared a numerically probe calibration of an ideal probe head geometry to four experimental calibrations of identical probes. The authors found that the four experimental calibrations deviated significantly, likely caused by manufacturing tolerances. Nevertheless, the numerical calibration of an ideal probe geometry showed good agreement with the experimental calibrations, but the static pressure at all side holes was underestimated. Schäffer et al. recommended using a scan of a probe to compensate for all geometry effects. Further, it was shown that modeling the probe holes itself leads to a much better agreement between numerical and experimental calibration.
Torre et al. [11] did a fully numerical investigation regarding vane-probe interactions. A numerically calibrated probe was placed behind a vane, and the results, calculated from the probe hole pressures, were compared to the undisturbed flow conditions. The differences between the undisturbed flow and the 5HP measured flow condition are due to the spatial dimension of the probe and the interpolation scheme.

The previous publications can be classified according to how accurately they reproduce the real probe geometry. The first group of studies [5], [6],[7], [8] and [12] used the ideal probe head geometry without modeling the probe holes.
In order to have a more realistic probe head, Schäffer et al. [10] modeled the probe holes of an ideal probe head. Lastly, Passmann et al. [9] projected the real location of the holes onto an ideal probe geometry. However, the holes were not modeled. Most previous investigations mentioned that the difference between numeric and experimental results may relate to differences in the geometry between the real probe geometry and the one used in the simulations. However, no previous study has assessed which geometric differences between the ideal probe and the real one drive the differences on the pressure measurements between numeric and experimental calibrations. Moreover, to the authours knowledge, no prior investigation has considered a real probe geometry combined with probe hole modeling. Such a configuration could potentially reproduce better the real flow conditions and therefore obtain a more realistic numerical calibration. Seeing this knowledge gap in the literature, the authors of this study set themselves to investigate this issue. Therefore, multiple geometries with a different level of adaption of the real probe

geometry are generated. An micro CT is used to generate a realistic model of a real probe including the inside of the probe holes. In the following, a numerical process using *Ansys Fluent 2024.R1* is established to generate numeric calibrations for all investigated geometries.

2 Experimental Setup

Different kinds of pneumatic probes are used for measurements in turbomachinery. All have a small spatial size and a low overhang in common to reduce the influence of the probe on the flow, and allow the mounting of the probe between two blade rows inside a turbomachine.

2.1 Probe Geometry

Pyramidic, conical, and spherical probe heads are commonly used in turbomachinery applications. This study investigates two probes with the same dimension (Figure 1 a) but different head shapes. At first, a conical probe's (Figure 1 b) measurement-reliability and calibration process is analyzed. The probe is used for measurements at LTF's High-Speed-Research-Compressor (HSRC). Later, a spherical probe (Figure 1 c) of identical size, used for measurements at a turbine-center-frame test rig, is numerically calibrated. The definition of yaw α angle and pitch β angle is shown in Figure 1 b).

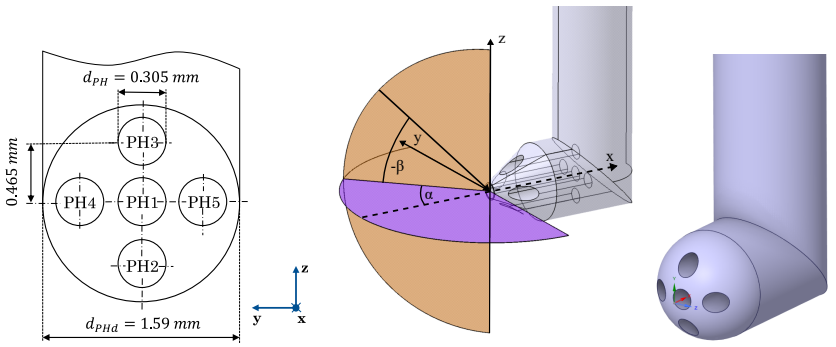

(a) PHd geometry (b) conical PHd, angle definition (c) spherical PHd

Figure 1 Nominal probe head geometry for conical and spherical probe, angle definition

2.2 Calibration Wind Tunnel

All pressure probes used in this investigation are calibrated in the free air stream of the calibration wind tunnel, known as Caljet, at LTF. The design of the settling chamber is shown in Figure 2. Pressurized air is provided by either the shop air pressure system (SAPS) or by a blower connected to the inlet of the wind tunnel (1). The SAPS provides an air flow with higher pressure and high mass flow rate, allowing Mach numbers up to $\mathrm{Ma}_{\mathrm{max}} = 1.3$ to be reached at the outlet of the described setup. The flow temperature is nearly independent of the outlet Mach number, but the achievable Mach number stability with the current setup is insufficient, especially for low Mach numbers. For low Ma-numbers up to $\mathrm{Ma}_{\mathrm{max}} = 0.65$, a blower is used. Using the blower as a source of pressurized air is preferable to get a more stable mass flow over the whole calibration range of the descriebed probes. The achieved Mach number stability is $\mathrm{Ma}_{\mathrm{variation}} = 0.00008$, independent of the operation Mach number. The flow temperature is not constant using the blower. The temperature variation was found in the range of $\Delta_{T,max} = 45\,K$, resulting in a negligible influence on the Ma-number.

Behind a perforated conical-shaped impact plate (2), a honeycomb (3) and multiple turbulence grids (4) - (8) are placed to reduce radial velocity and turbulence. Downstream in the flow conditioning zone (9), the temperature is measured using two Resistance Temperature Detectors (RTDs) (10). In the same region total pressure is measured (11) at two positions. Throughout the contraction zone (12), the flow is accelerated to the desired Mach number, and leaves the settling chamber

through the nozzle (13). The static pressure is measured in the nozzle exit plane (14) to detect blockage. The diameter of the free-jet nozzle is $d_{Nozzle} = 25.4\,mm$. Whenever a probe is calibrated, it is placed 40 mm behind the nozzle to avoid blockage. The ratio of the probe head- to nozzle diameter of the probes used in this study is 1 : 16, and the blocked area of the free-jet, including the stem of the probe, is 4.18 %. The traversing system is a three-translatoric and two-rotational traversing system. Yaw angles of $\alpha_{max} = \pm 180°$ and pitch angle between $\beta_{max} = 45°$ and $\beta_{min} = -90°$ can be achieved.

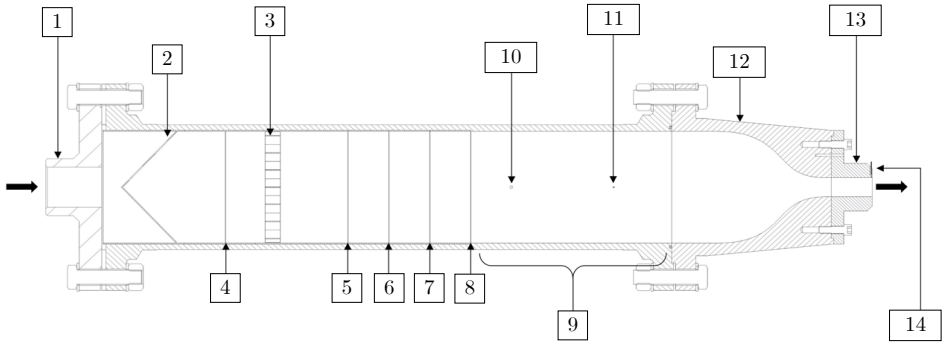

Figure 2 Design of Caljet

2.3 Calibration Coefficient

A 5HP needs to be calibrated before it can be used to measure flow quantities during a test. For this calibration, probes are placed at LTF's Caljet and are rotated at different flow Mach numbers. The calibration conditions are defined in Table 1:

Table 1
Calibration conditions

	min	stepsize	max	Unit
Mach number	0.1	0.1	0.6	-
yaw/pitch angle	-2.5	0.25	2.5	deg
yaw/pitch angle	-5	0.5	5	deg
yaw/pitch angle	-10	1	10	deg
yaw/pitch angle	-30	2	30	deg

One calibration consists of approximately 12.000 calibration points. The small step size in yaw and pitch for small flow angles is defined to reduce interpolation errors. The used settling- and measurement- time varies from one probe to another, and it is usually between $4\,s < t_{settling} < 12\,s$, and $2\,s < t_{measurement} < 4\,s$. This leads to a calibration time of $20\,h < t_{calibration} < 53\,h$. The calibration process is fully automated, and the Caljet operates entirely autonomously.
In the context of this study, the calibration coefficients are, in agreement with [10], defined as follows, where the naming of the probe holes can be seen in Figure 1 a:

$$C_{yaw} = \frac{P_{PH5} - P_{PH4}}{P_{max} - P_{avg}} \tag{1}$$

$$C_{pitch} = \frac{P_{PH3} - P_{PH2}}{P_{max} - P_{avg}} \tag{2}$$

$$C_{P_t} = \frac{P_t - P_{PH1}}{P_{max} - P_{avg}} \tag{3}$$

$$C_{P_d} = \frac{P_t - P_{ref}}{P_{max} - P_{avg}} \tag{4}$$

$$P_{max} = \frac{P_{\mathrm{PH1}} + max(P_{\mathrm{PH1-PH5}})}{2} \tag{5}$$

$$P_{avg} = \frac{P_{\mathrm{PH2}} + P_{\mathrm{PH3}} + P_{\mathrm{PH4}} + P_{\mathrm{PH5}}}{4} \tag{6}$$

2.4 Error Estimation

For measuring the 5HP pressures, a differential DSA3217 from *Scanivalve* is used. The pressure range of the device is 5 psi (34474 Pa) differential with a nominal full-scale accuracy of 0.05 %, which corresponds to a device-error of approximately $\mathrm{e_d} = 17\,\mathrm{Pa}$. The pressure samples taken in this study have a maximum standard deviation of $\sigma_\mathrm{p} = 4\,\mathrm{Pa}$. The used absolute pressure sensor *Mensor* CPT6020 has a range of 1.3 bar with a full-scale accuracy of 0.02 %, which corresponds to a device-error of $\mathrm{e_a} = 26\,\mathrm{Pa}$. Since the calibration certificate of the ambient pressure sensor indicates a maximal error of 0.002 %, a pressure error of $\mathrm{e_a} = 2.6\,\mathrm{Pa}$ is used for the error estimation. Two CPT6020 sensors are used and averaged to calculate the correct absolute pressure.

This leads to an absolute pressure error of each probe hole pressure of:

$$\Delta e = \sqrt{{\mathrm{e_d}}^2 + \sigma_\mathrm{p}^2 + {\mathrm{e_a}}^2} = 17.85\,\mathrm{Pa}. \tag{7}$$

The pressure error is the same for each measured pressure P_i occurring in equations 1 to 4. Each calibration coefficient equation contains four pressures P_{i1} to P_{i4}, which can be, depending on the calibration coefficient, P_t, P_{avg}, P_{max} or P_{PH1} to P_{PH5}. The experimental error of each calibration coefficient, C_i, can be calculated according to the error propagation equation derived from Taylor [13]:

$$\Delta E_{\mathrm{C_i}} = \sqrt{\left(\frac{\partial C_i}{\partial P_{i1}} \cdot \Delta e\right)^2 + \left(\frac{\partial C_i}{\partial P_{i2}} \cdot \Delta e\right)^2 + \left(\frac{\partial C_i}{\partial P_{i3}} \cdot \Delta e\right)^2 + \left(\frac{\partial C_i}{\partial P_{i4}} \cdot \Delta e\right)^2}. \tag{8}$$

A Monte Carlo analysis, similar to Hölle et al. [14], is conducted to calculate estimated errors of the resolved flow angles. The error resulting from misalignment, instrumentation errors, and interpolation are $\alpha/\beta_{error,CI97} = \pm 0.22°$ for a confidence interval of 97%.

2.5 Difference between Calibration and Compressor Testing Environment

A test (yaw-check) is conducted to understand the reliability of the angle measurement with a 5HP inside a compressor (see Figure 3). Therefore, three new calibrated conical 5HPs (see Figure 1 b) are placed in LTF's 3.5 stage HSRC behind each rotor blade row at mid-span (Ma $\approx$ 0.50), aligned with the metal angle of the rotor and rotated by $yaw = \pm 15°$ in $\Delta_{\mathrm{yaw,HSRC}} = 1°$ steps. An internal sensor in the stepper motor measures the yaw position. Since the difference between the measured and the set position is small (e.g. $\Delta_{\mathrm{max,angle}} < 0.002°$), the positioning error is neglected. Later, the angle measured by the 5HP's is compared with the actual measured angle from the encoder, deriving the corresponding measurement errors for misaligned probes.
Additionally, the probe placed behind R2 is placed in the caljet at a similar Mach number (Ma = 0.50) and rotated by $yaw = \pm 15°$ in $\Delta_{\mathrm{yaw,caljet}} = 0.1°$ steps.

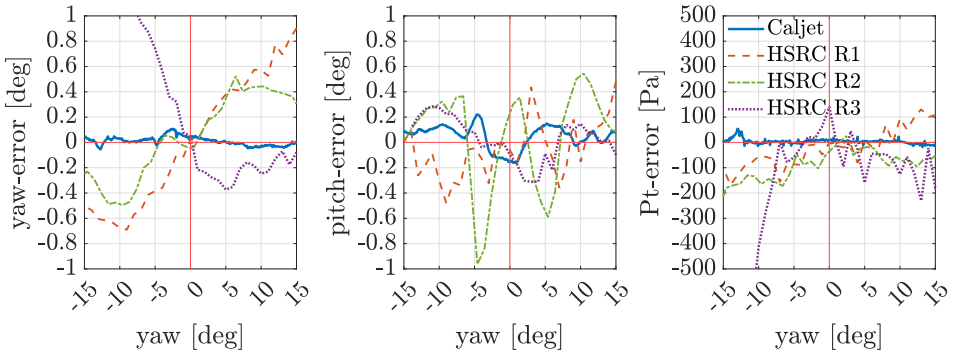

Figure 3 Yaw-check

Figure 3 shows the measured and processed data. The yaw-check in the caljet shows averaged errors of $yaw_{\text{set}} - yaw_{\text{meas}} = \pm 0.028°$, $pitch_{\text{set}} - pitch_{\text{meas}} = \pm 0.090°$, $\text{Ma}_{\text{set}} - \text{Ma}_{\text{meas}} = \pm 0.00041$, $P_{\text{s,ref}} - P_{\text{s,meas}} = \pm 23\text{Pa}$ and $P_{\text{t,ref}} - P_{\text{t,meas}} = \pm 7\text{Pa}$.
In contrast, the yaw-check in the compressor shows significant errors, which are strongly dependent on the mounting position or probe.
The reason for this may relate to the high turbulence, unsteady effects behind a rotor, steady effects of the stator downstream, or the change in Reynolds number ($\text{Re}_{\text{probe,R3}} = 1.8 \cdot \text{Re}_{\text{probe,caljet}}$) compared to the calibration. The exact source can not be evaluated, but if the flow around the probe can be replicated in numerical simulations, the effects can be investigated separately. This can help to understand how these measurement errors occur and also help to introduce new corrections. Section 4 provides a guideline on how simulations of this kind can be conducted.

3 Geometries used for Numeric Investigation

In this paper, multiple probe geometries are investigated.
The simplest geometry is the ideal probe geometry from the technical drawing of the probe, following Figure 1 a, without modeling the probe holes. This approach was used by [5], [6],[7], [8] and [12] to do numerical investigations on pressure probe heads. This geometry is referred to as **wo PH** (without probe holes) and is shown in Figure 4 a.

The next level of refinement is generated by including the probe holes (internal ducts) in the CAD model. This is the same approach Schäffer et al. conducted in [10]. Following Schäffer, the total and static pressure should be captured better if the probe holes are modeled. This geometry is referred to as **w PH** (with probe holes) and is shown in Figure 4 b.

An additional geometry is generated by combining the approaches of Schäffer et al. [10] and Passmann et al. [9]. Passmann did an optical 3D scan of a probe head and generated a CAD model following the 3D Scan. The probe holes in [9] were not modeled but were projected from the scan on the ideal geometry to get the exact probe hole position for the numerical investigation. In this paper, a CAD model is generated by placing the probe holes at the precise position of the real probe, using pictures from a microscope. Since Schäffer et al. [10] showed the importance of modeling the probe holes, the probe holes are also modeled in the investigated geometry. Further, the probe head is scaled to the measured diameter of the probe head. This geometry is referred to as **w PH pos** (with probe holes positioned) and is shown in Figure 4 c. The ideal PH position is shown in red, while the real PH position, following the microscope, is white.

With a scan of the probe head, a new kind of geometry is investigated. The scan generation is described in the following subsection. This geometry corresponds to the best possible and available adaption of the real geometry. The probe holes are

included in the 3D scan. This geometry is referred to as **scan** (real geometry 3D Scan) and is shown in Figure 4 d.

Since the raw 3-D Scan shows a rough surface, most likely a result of beam hardening of the polychromatic X-ray spectrum in the scanning process, an additional geometry is generated. Therefore, the surface of the probe head, but not the inlet of the probe hole, is smoothed to replicate the real probe surface better. This geometry is referred to as **scan smooth** (real geometry 3D Scan with smoothed surface) and is shown in Figure 4 e.

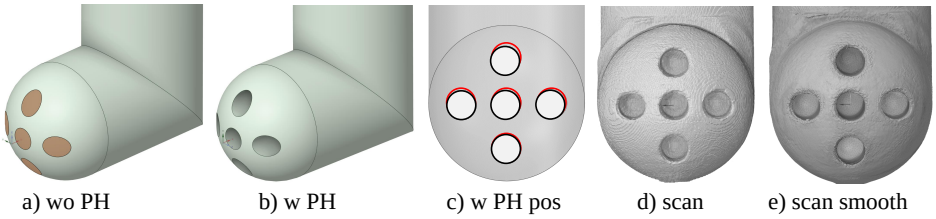

Figure 4 Investigated geometries

3.1 Real Geometry Scan

Optical measurements, like laser-based or microscope-based measurement techniques, are commonly used to map the surface of objects on interest, and could potentially be used to retrieve the probe real geometry. However, since the optical access to the probe holes is limited, not all geometry features can be mapped. Also, the high-resolution requirements for the small geometry can not always be achieved.

To overcome this issue, a micro CT (Computer Tomograph) *"v|tome|x s 240"* is used. A micro CT uses X-rays to generate information about the density and elemental distribution of an object. Using that information, a 2-D cut-plane through the probe can be generated with the linear attenuation factor for a greyscale. By defining a threshold in *Matlab*, 1000 of these 2-D cut-planes can be used to generate a full 3-D model of the probe using *ImageJ*. Since the *"v|tome|x s 240"* is not a metrological micro CT, the size of the probe is scaled to the size determined with a dial gauge.

Figure 5 shows the scanned probe geometry, and its deviation with respect to the ideal geometry.

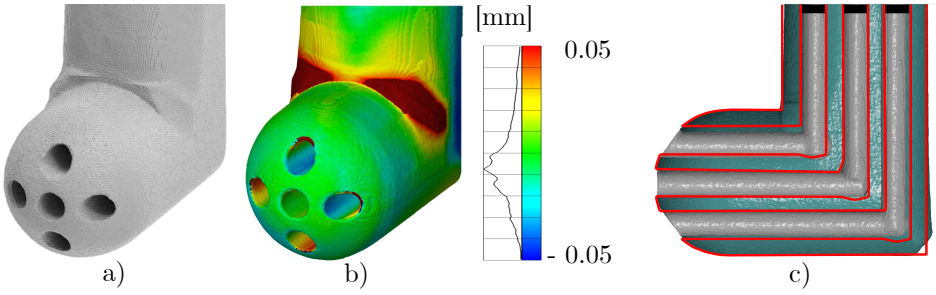

Figure 5 a) Scanned geometry b) Deviation to ideal geometry c) Cut through the scanned geometry (read lines indicate location of ideal probe inner ducts)

Deviations between ideal and scanned geometry can be seen at multiple locations. Maximal deviation is seen at the junction between the probe head and probe stem in Figure 5 b. This feature may influence the pressure measured with PH3 due to its proximity and, consequently, C_{pitch}. The dynamic pressure coefficient C_{pd} may also be influenced, since for its calculation the pressure measured at PH3 is used. Further, the location of probe holes on the probe head differs from the ideal geometry (following Figure 5 c). Later, it will be seen that the probe hole position has a profound effect on the calibration outcome.

Additionally, differences in the radius around the probe holes are present (Figure 5b, red area around the probe hole). The drawing is considered to have a sharp edge, which is not visible in the scan.

It has to be mentioned that, especially for the conical probes, a large metallic burr is seen at the entry of the probe holes. Such burr is an artifact of manufacturing, and tends to appear in regions of small wall thickness (e.g. at the outer edge of PH2-5). Since this burr has sharp edges and its wall thickness is very thin, it is likely to change over time. If that happens, the inlet of the probe hole will be enlarged, and by that, the calibration of the probe will be changed (see section 5). Therefore, it is important to re-calibrate probes (also new ones) and further investigate the aging effects of probes.

4 Numerical Process

The numerical procedure in this paper is strongly related to the approach recommended by Schäffer et al. [10]. The reader is refereed to the work of Schaffer et al for a detailed explanation of their approach. Nevertheless, minor changes are conducted to make the process better suited for simulating 3D-scanned geometries. For instance, a real geometry scan's meshing is way more time-consuming compared to the w PH geometry Schäffer et al. used in [10]. Therefore, the approach of generating a mesh for each yaw- and pitch-angle combination to reduce numerical errors is rejected. Only one mesh is generated, and the flow is rotated by changing the flow condition at the boundary conditions (BC). *Ansys Fluent 2024.R1* is used for meshing and solving the simulations. All details, including any deviation from the procedure followed by Schaffer et al, are described in the incoming sections.

4.1 Domain

The geometry (e.g., wo PH, w PH, w PH pos, scan or scan smooth) is placed in a box with a length of each edge of $160 \cdot d_{probe}$ which equals 256 mm. Schäffer et al. [10] recommendations are taken into account. For the real geometry case, the geometry should be cleaned off any artifacts generated during the CT scan. These should be separated and deleted in the pre-processing of the geometry. Additionally, it needs to be checked whether artifacts connected to the probe geometry are located in the probe holes. These could lead to a failure in the meshing process since the boundary mesh layer can not be generated correctly.

4.2 Meshing

In the following, an overview of the settings for mesh generation is given. It is essential to state that meshing a scanned geometry is challenging. While generating the mesh of an ideal geometry takes less than 10 min, the mesh generation for the scanned geometry takes approximately 8 h. As stated, *Fluent Meshing*, featuring its poly-hexcore meshing option, is used. *Ansys* provides a detailed explanation of this function in [15].
Three density regions are placed in the domain. Two conical cylinders with an opening angle of 60° are placed around the probe head to cover up the following effects:

- Stagnation of the flow in front of the probe (comparable to [10]) but for varying flow angle.
- Capturing the near probe wake, which could influence the probe hole pressures.
- Capturing the far probe wake to reduce the residuals in the overall simulation.

Additionally, a sphere with a diameter of 5 mm is placed around the probe head to cover all effects closely around the probe head, like separation and stagnation

of the flow in front of the stem.

A mesh independence study on the scanned geometry is conducted to investigate the mesh dependency of the probe hole pressures. The meshes are generated following the guidelines from the Journal of Fluids Engineering [16]. Using the GCI approach, characteristic values Φ_i for the simulation are extrapolated, Φ_{21}^{ext}, to better describe the errors caused by the limited discretization of the flow field. The mesh study is conducted at a flow angle of 0° in yaw and pitch at Ma = 0.3 . First, the boundary layer cells are defined to provide $y^+ < 1$ on the probe surface for all simulations. Secondly, mesh parameters like face size on the probe surface, and resolution in the density regions are varied to determine the size of the mesh. Three meshes are generated for the convergence study, and their effect on the results is assessed by evaluating the resulting probe hole pressures $\mathrm{PH1-5} = \Phi_i$. Table 2 shows information about the investigated meshes, the derived probe hole pressures, and the significant parameters following [16].

Table 2
Mesh study - GCI parameters

Mesh	**Cell No.**	r_{21}	r_{32}	Φ_1 [Pa]	Φ_2 [Pa]	Φ_3 [Pa]	Φ_4 [Pa]	Φ_5 [Pa]
M1	36 Mio	1.31	-	6173	2420	5120	3357	3472
M2	16 Mio		1.47	6174	2422	5120	3358	3476
M3	5 Mio	-	-	6177	2508	5127	3428	3535

Φ_i	Φ_{21}^{ext}	$e_{21}^{abs-ext}$	GCI_{21}
Φ_1	6173	1	0.0077 %
Φ_2	2420	2	0.0015 %
Φ_3	5120	0	0.0036 %
Φ_4	3357	2	0.00030 %
Φ_5	3472	0	0.0071 %

Given the results provided in Table 2, it can be concluded that a mesh of 16 Mio cells provides a sufficient spatial discretization of the flow field. Since all geometric features of the probe should be covered in this publication, a finer mesh with 26 Mio cells is used for all simulations with the scanned geometry.

4.3 General Settings

In this section, the general simulation settings in *Fluent 2024.R1* are shortly described. All simulations are carried out as RANS-simulations since Schäffer et al. [10] described this as sufficient. The operating pressure (comparable to an ambient pressure) is defined to be the same as during the experimental calibration. The SST-based GEKO-turbulence is used to model turbulence [17] to enable the adaption of the turbulence model based on the good available experimental data. This may be done in future investigations. The fluid density is derived from the ideal gas law, so the simulations are carried out for a compressible gas. Second-order upwind schemes are used for spatial discretization. To follow the simulation convergence, a surface at the end of the modeled probe hole is generated. The area-averaged pressure is monitored during the simulation and convergence is considered to be achieved when the maximum deviation within 30 timesteps is below 1 [Pa]. The locally scaled residuals of all governing equations must also be lower than 10^{-5}. A user-specific time step is defined to provide optimal convergence.
Since the numerically definable errors (mesh and convergence) are small (see $e_{21}^{abs-ext}$, Table 2), no error bars will be added to numerically gained data.

4.4 Probe alignment

In experiments, a reference surface at the end of the probe is used to align the probe. This surface is not included in the scan, so another way needs to be found to align the probe in a way similar to the experiment. Therefore, the real probe is simulated at an incidence of approximately yaw = pitch = 0°. The pressures in the probe holes (PH1-PH5) are post-processed using an experimental calibration. Then, the probe is turned by the resolved angles to compensate for the misalignment, the probe is meshed and simulated again, and the resulting

flow angles are checked. As soon as flow angles $< 0.01°$ are reached, the probe is considered aligned similarly to the experiment. This approach only works if an experimental calibration for the probe is available and the simulated geometry agrees with the real geometry.

5 Results

A series of simulations is conducted for each of the previously described geometries. The Mach numbers tested are Ma $= 0.2, 0.3, 0.4, 0.5, 0.6$. At each Mach number, the yaw and pitch angles are varied from $-12° <$ yaw /pitch $< 12°$ degrees. This results in total number of 125 simulations.
For the sake of brevity, only the results obtained with a Mach 0.3 are presented, as they are representative of the results obtained at Mach numbers Mach Ma $= 0.2, 0.3, 0.4, 0.5$. It should be highlighted though that the pressure in PH3 differs slightly from the experimental data at higher Mach numbers Ma $= 0.6$. Additionally, convergence at Ma $= 0.2$ required more effort.
In the next section, the resulting calibration coefficients obtained at Ma $= 0.3$ for all geometries are explored. Out of this analysis, the best performing geometries are selected. Then, for each one, the performance of the numerical calibration is assessed. later, the flow around the best performing probes is further investigated in detail.

5.1 Analysis of geometry modeling on numeric calibrations

The aim of this initial study is to determine the effect of geometry accuracy, i.e. how well the real probe geometry is replicated, on the calibration coefficients. For that purpose, a numerical calibration at Ma $= 0.3$ is conducted for each one of the probes presented in Section 2.1. Then, the numerical calibration coefficients are compared with those obtained experimentally. All geometries described in Section 3 are meshed with the same settings, only the geometries based on the Micoro CT scan require a more refined mesh. Further the same simulation setup is used. All simulations' calibration coefficients are calculated following the previous definition in Section 2. Error bars for the experimental data are calculated following Taylor [13] as described in Section 2. Figure 6 shows the calibration coefficients for yaw and pitch angles in a range of $\pm 12°$.

The geometry **wo PH** disagrees with the experimental data. The total pressure coefficent is strongly overestimated caused by an underestimation of the pressure in PH1, as predicted by [10]. Further, all pressures at PH2-4 are underestimated, leading to a too-low C_{pd}. The angle coefficients are also not properly met.

The geometry **w PH** shows good agreement for C_{pt}. The shape of the other calibration coefficients is better covered but with a significant offset. Especially C_{pd} and C_{pitch} are underestimated. It can be noted that C_{yaw} is zero for all perfect symmetric probes (wo PH, w PH) during pitching, as it should be, following the coefficient definition in Section 2.

The geometry **w PH pos** agrees well with the experimental data. The total pressure coefficient C_{pt} is met within the experimental accuracy. Compared to the symmetric geometry, the angle coefficients only show slight deviations from the experimental data. Notably, C_{pd} is met within the measurement accuracy for most angles. Differences in C_{yaw} during pitching are seen.

The **scanned** geometry agrees well with the experimental data. All coefficients agree with the experimental measurement accuracy for most angles. Only C_{yaw} during pitching and C_{pitch} during yawing show small deviations. Over all, significant improvement for the behavior of C_{yaw} during pitching compared to w PH pos is seen. This may be caused by the additional geometry feature at the junction of the probe head and the stem (Figure 4). The geometry **scan smooth** behaves

similarly to the scan geometry.

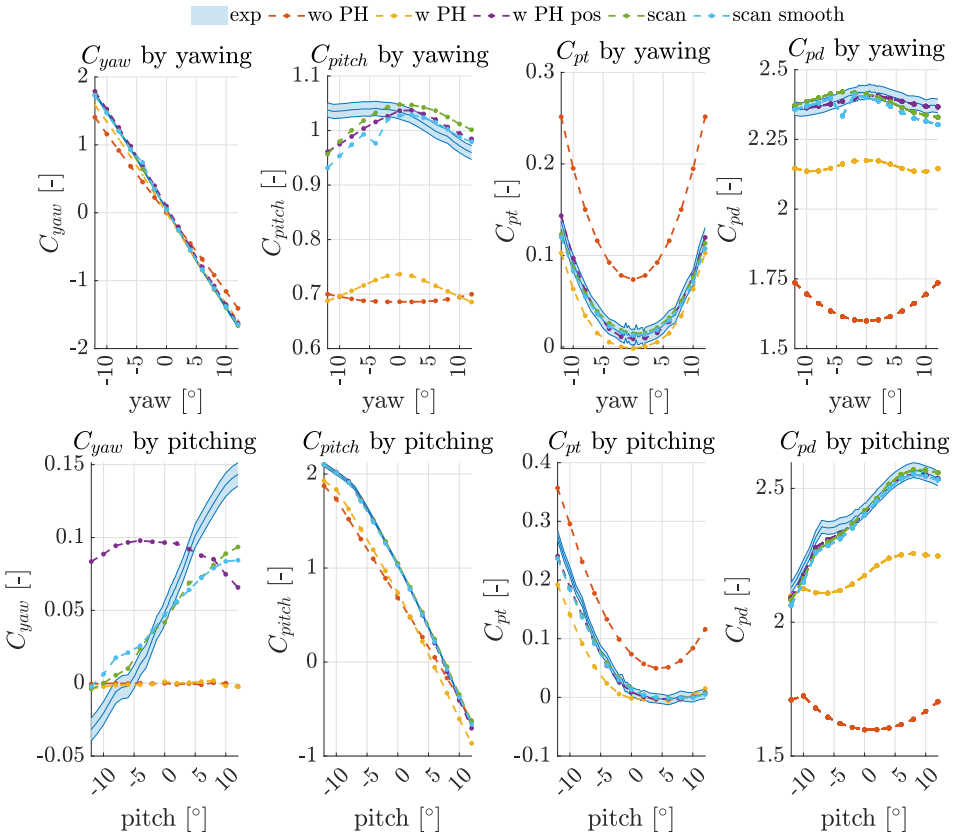

Figure 6 Comparison of Calibration coefficients

It can be stated that the the more realistic the probe geometry is, the better the data produced by the simulations agrees with experimental data. The outcomes exhibit a high sensitivity to geometric parameters, as posited by previous papers. Small adaptions in the investigated geometry, including the modeling of probe holes (as recommended by [10]), gain a huge improvement. Using microscopy pictures of the probe head to place the modeled probe hole in the correct position and scaling the probe to the real diameter especially improves the static pressure measurement.

5.2 Performance of Numeric Calibration

In the previous section, it has been seen that the w PH pos, scanned, and smooth scanned probes yield numerical coefficients that are overall in fairly agreement with the ones obtained experimentally. Nonetheless, it is important to verify whether the numerical calibration done with these geometries could substitute or extend the experimental calibration for flow conditions not reachable with experiments.

Therefore, the numerically generated probe hole pressures are post-processed using the experimental calibration. The results are compared to the flow condition during the simulation. Following that, an order of magnitude for the errors made while using an experimental calibration for numerically generated data and vice versa is given.
Figure 7 shows the averaged errors, calculated from the flow condition defined in the simulation and the flow condition measured by the 5HP for $-12° < \text{yaw/pitch} < 12°$.

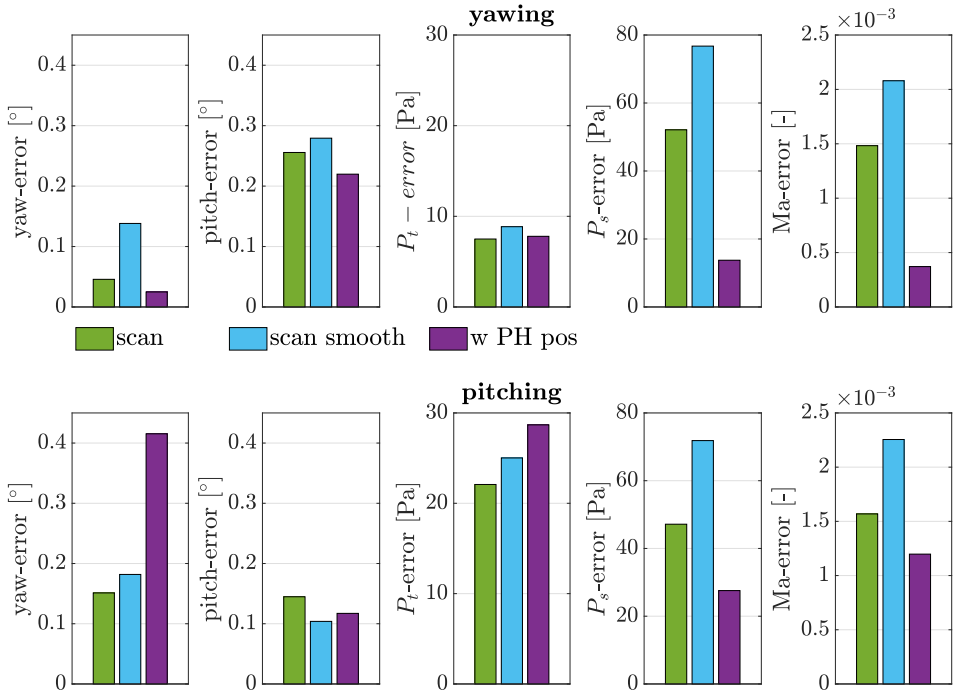

Figure 7 Differences from numerical and experimental data

It can be stated that the scanned and the w PH pos geometry perform best. Averaged yaw errors of 0.04° and static pressure errors below 50 Pa ($Ps_{error,abs} \approx 0.052\%$) at Ma = 0.3 ($Ma_{error} \approx 0.5\%$) are considered sufficiently small. The average error is to be found in a similar range compared to the conical probe investigated in the caljet shown in Figure 3. Similar to the yaw test at the caljet (section 2), it can be seen that the pitch error while yawing is high. This follows from the flat platon of C_{pitch} (also seen in Figure 6) during yawing, where small pressure deviations can strongly impact the resolved angle. The same applies to the yaw angle during pitching. Further, it can be stated that smoothing the surface of the probe head does lead to a worse performance compared to experimental data. Therefore, this approach is dropped for the rest of the paper.

For a deeper understanding, especially for the angle dependency of the errors, Figure 8 shows the resolved data for multiple angles. Only the scan and w PH pos geometries are shown, since the scan smooth geometry does not show any improvement.
The w PH pos geometry simulations provide good results for all flow quantities. Since the w PH pos geometry is not aligned with the experimental calibration, a constant offset of offset = 0.30° is subtracted from the resolved yaw angle. All errors, especially for flow angles < 10°, are considered sufficiently small.
Since the magnitude of the errors is comparable to experimental tests, it can be stated that the described numerical process can generate a high quality calibration map. The numeric calibrations using both geometries can be used to post-process experimental data without losing accuracy. Additional calibration data for flow conditions that cannot be reached experimentally can be generated numerically.

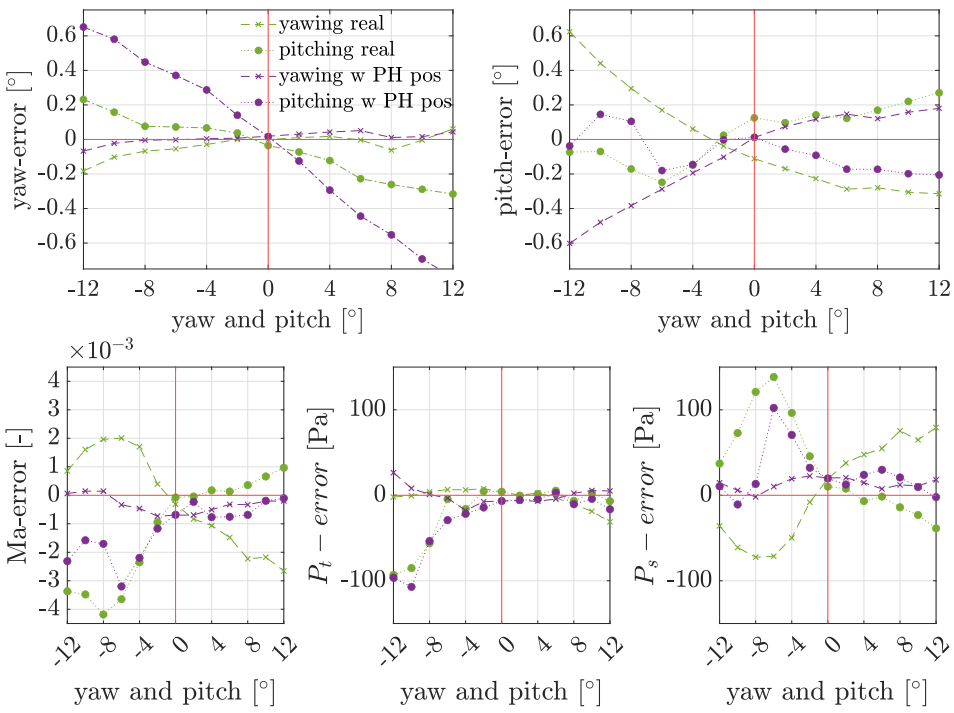

Figure 8 Measurement error during variation of incidence

5.3 Flow Field Analysis

To better understand the flow field around the probe head, further investigations are carried out. In Figure 9, streamlines on the probe surface and the skin friction coefficient for the w PH pos (a) and scanned (b) geometries at yaw = pitch = 0° are shown.

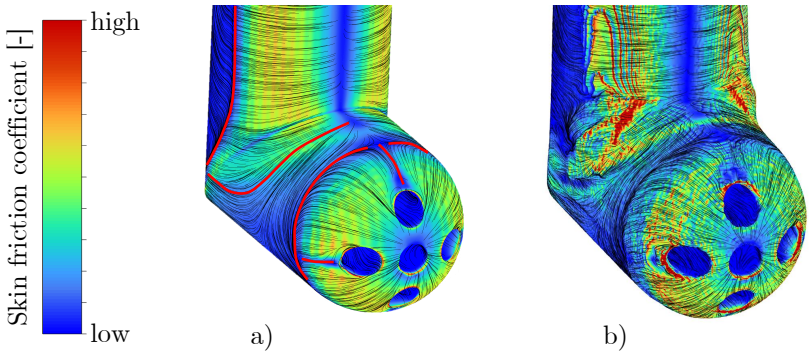

Figure 9 Streamline at probe surface a) w Ph pos, b) scan

Overall, the streamlines of the two geometries are in good agreement. Separation areas are marked as red lines. Both geometries show separation at each of the probe holes downstream corner. Also, separation is seen at the transition of the spheric to the cylindrical part. At the top side of the probe head, the flow is reattached and pushed aside by the potential field of the stem. A horseshoe vortex is formed at the top of the probe head and pushed down on both sides alongside the probe. Separation can also be seen at the stem.

Differences are seen in areas with sharp corners. The sharp edge at the probe hole of the ideal geometry provides a small area of high skin friction coefficient, while the bigger radii at the scanned geometry shows a higher skin friction coefficient and a larger follow-up separation area. The stem and probe head junction feature (see Figure 5) causes an additional vortex directly above the horseshoe vortex. The original horseshoe vortex is pushed down further at the scanned geometry.

To have a better understanding how the measured pressure is applied to the probe head, the surface pressure distribution is illustrated in Figure 10 for Ma = 0.3 and at yaw = pitch = 0°. Figure 10 a and b are a comparison of the static pressure distribution of the w PH pos geometry and the scan geometry. The pressure distribution is similar for both geometries. Small differences are seen downstream of the probe hole. Also the pressure distribution directly around the PH is different, driven by the radius or/and the burr covered by the scan geometry. Further a strong dependency of the static pressure on the position on the spherical probe head is seen. This is an explanation for the w Ph pos geometry performing significantly better than the w PH geometry (cf. Figure 6). Figure 10 c shows the static pressure distribution in the pitch plane and on the probe surface of the scan geometry. Due to the acceleration of the flow at the lower portion of the probe head, separation is triggered at the downstream corner of PH 2 (cf. Figure 1 a). The static pressure field for both probe geometries (Figure 10) show a shift of the stagnation point upwards, towards the stem. This is caused by the potential field of the stem. The similarity in the pressure field is coherent with the good agreement of the two geometries in the calibration coefficients (Figure 6).

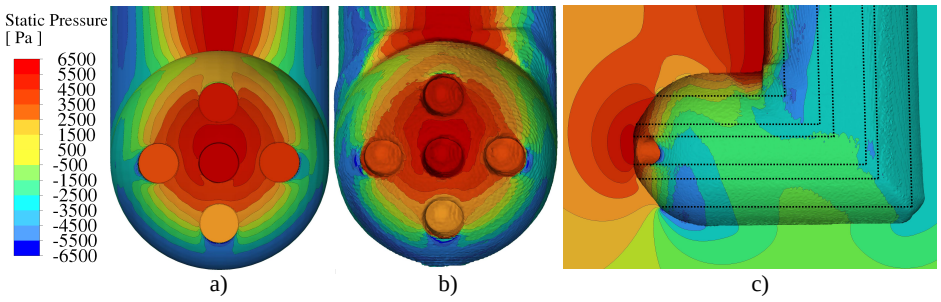

Figure 10 Static pressure distribution on probe head a) w PH pos b,c) scan

In order to have a better understanding of the flow around the probe head, the dependency of the velocity field with angle of incidence is analyzed. It must be stated that vortexes are not a stationary phenomena and can not be fully described by steady-state simulations. URANS simulations were not considered given the computational cost required to run each calibration point. However, RANS simulations are a reasonable indicator of the time average features of the different vortex at play.

First, the cutting plane approx. trough PH1, PH4, and PH5 (z-plane) is investigated during yawing. The velocity magnitude and streamlines for yaw = 0°, yaw = −10° and yaw = −20° are shown in Figure 11 for the scaned geometry. The unique shape of the scan geometry, including the radii at the probe hole inlet, is visible. At the side holes, the flow enters the probe holes at the outer part of the probe hole. The flow is turned, and a vortex structure forms before the flow leaves the probe hole in the inner area. The change of yaw angle causes a shift on the stagnation point that leads to a change in the vortex structure inside the probe holes. The vortex structure in the side hole more aligned with the flow (PH5) becomes less complex and the rotational energy decreases. In contrast, the probe hole less aligned with the flow shows a stronger and more complex vortex structure.

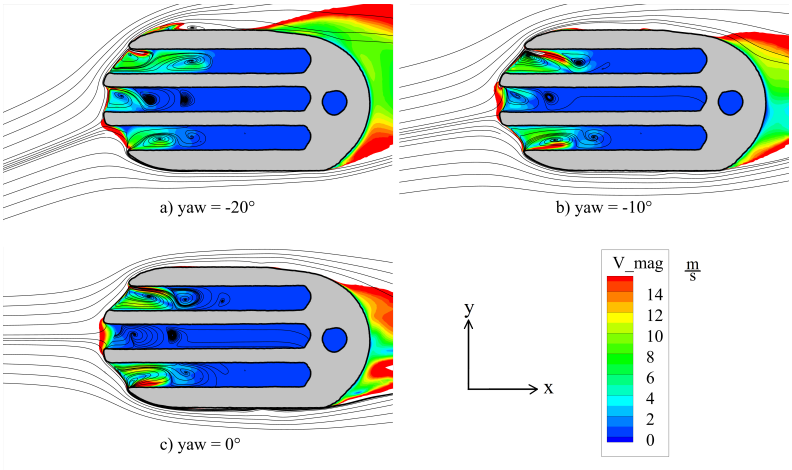

Figure 11 Velocity and streamlines inside probe holes in z plane during yawing of scaned geometry

To show the influence of pitch-variation on the flow field Figure 12 is provided. Since the influence of pitch can not be considered to be symmetric, positive and negative pitch angles of $\pm 20°$ are investigated. Due to the potential field of the stem, the streamlines are bent slightly in negative z-direction for pitch $= 0°$ (Figure 12 c). Also, the stagnation point for this flow condition is shifted to the upper portion of PH1. Through additional negative pitch, the stagnation point is moved directly on PH3 (for yaw $= -20°$). Inside the probe hole, a strong vortex is formed, neglecting any flow entering the probe hole. This behavior is also seen for small positive pitch angles in PH1. Again, the vortex inside the probe hole, less aligned with the flow, strengthens. Separation happens at the probe's lower side, triggered by the outer edge of PH2. At this point, a recirculation bubble can be observed. For a pitch $= 20°$ the stagnation point is not moved far enough downwards to reach fully PH2. The strength of the vortex in PH2 is reduced, but not to the level of PH3 at pitch $= -20°$. A strong vortex structure is seen in PH3. Further investigations of the geometry w PH pos show that the sharp edge of the probe hole catches the flow better and stabilizes the stronger vortex structure. For a detailed analysis of the flow at a probe head, it is important to have an exact replica of the tip of the probe head.

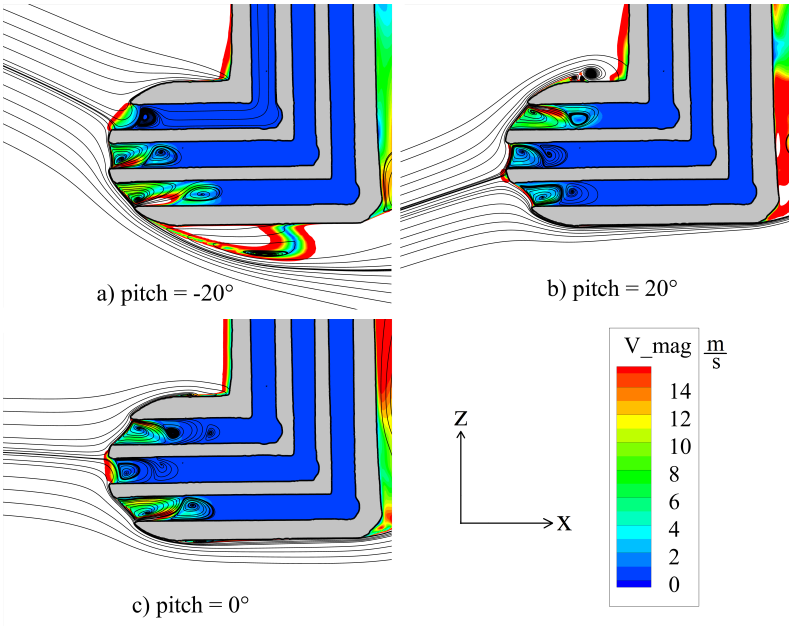

Figure 12 Velocity and streamlines inside probe holes in y plane during pitching

A vortex is always coupled with a pressure loss caused by entropy generation. Therefore, the vortex's size and strength impact the pressure measured at the probe hole. The amount of entropy generated inside the probe hole correlates with the size and strength of the probe hole vortex. Investigation at different Mach numbers shows that the strength of the vortexes for the same incidence varies with the free flow velocity. For higher Mach numbers, high velocity and strong vortex structures inside the probe holes can be seen. Following that, more entropy is generated, and the pressure loss is considered to be higher, affecting the resolved probe hole pressure more. This effect can be considered small for incompressible flows since the velocity, and, therefore, the entropy generation inside the probe hole, is small. In Figures 11 and 12, the dependence of the vortex from the flow angle is shown. In a compressor, the vortex inside the probe hole is not only affected by misalignment (see Figure 11 and 12, covered by the calibration) but also by unsteady flow effects, turbulence, and changes in Reynolds number compared to the calibration. So, these flow conditions influence not only the flow around the probe head but also the flow inside the probe holes. The impact of these vortexes needs to be further investigated.

6 Conclusion and Outlook

First, an experimental investigation of the measurement errors for misaligned probes in a 3.5-stage axial compressor behind each rotor blade row is carried out. The errors are known to be caused mainly by turbulence, unsteadiness, potential, and Reynolds number effects. This underscores the significance of enhancing the understanding of measurement errors during measurements with 5HP's.
A methodology for numerical calibration of pneumatic probes is introduced. A numerical investigation is conducted to understand the influence of geometry modeling of 5HP on the outcome of a numerical calibration. The most common approach, modeling the probe head (without probe holes) following the technical drawing, did not show good agreement with experimental data. Modeling and positioning the probe holes according to microscopic pictures and scaling the probe to a measured diameter reduces the differences between numerical and experimental data extremely. It can be stated that an ideal geometry with positioned probe holes can be used to generate numerical calibration data of experimental quality. Deviations of ($\text{angle}_{error,mean} < 0.19°$; $P_{s,error,mean} < 20\,\text{Pa}$; $P_{t,error,mean} < 18\,\text{Pa}$ at flow-angles yaw/pitch $= \pm 12°$ and $\text{Ma} = 0.3$) can be reached. A well-working methodology for the numerical calibration of pneumatic probes is introduced.

Besides ideal geometries, a micro CT was used to generate a 3D scan of the probe, including the inner geometry of the probe holes. Differences compared to the ideal geometry are seen for the probe hole position, the probe hole radii, and the junction between the probe head and stem. Additionally, probes have been seen to have a burr at the outer portion of the probe hole entry. The numerical calibration shows similar results as the ideal geometry probe with positioned probe holes, with the difference that the Cyaw coefficient is represented better by the scanned geometry. The scanned geometry, as well as the ideal geometry, was used to generate numerical calibration data. The numerical calibration shows similar results as the ideal Geometry with positioned probe holes.

The effort and cost of a full numeric calibration comparable to an experimental calibration is considered too high. However, since the flow condition inside a turbomachine is way more complex compared to calibration, additional data for flow conditions not or hardly achievable experimentally (e.g., Reynolds number, turbulence, unsteadiness, etc.) can be generated numerically. New corrections and more dimensional calibration methodologies (including Reynolds number or turbulence) could be introduced using that information. Further, aging schematics of pressure probes can be numerically investigated by manipulating the scanned geometry.

A flow field analysis provided insights into the complex vortex structures and their behavior inside probe holes, emphasizing their impact on pressure measurements. The importance of using the real, scanned geometry of the probe head for such investigations is shown.

In conclusion, this paper contributes valuable insights into the calibration and numerical simulation of pneumatic probes, offering guidance on improving accuracy through detailed geometric representations. The findings enhance the understanding of the challenges and opportunities in flow measurements in turbomachinery, paving the way for more reliable and precise experimental and numerical analyses in the field.

ACKNOWLEDGMENTS

The authors gratefully thank Dr. Massimiano Cirri from GE Aviation for his continuous great support, extremely helpful discussions, and sharing of expertise. Thanks are also due to Dr. Klaus Achterhold from the Chair for Biomedical Physics at TUM for providing the micro CT scans of various probes. Further, the authors thank Patrick Steudel and all the colleges that supported the authors during the investigation.

REFERENCES

[1] A. Appukuttan, R. J. Miller, and H. P. Hodson, "Probe Measurement Errors Caused by Shear Flows," *Symposium on Measuring Techniques in Transonic and Supersonic Flow in Cascades and Turbomachines*, no. MTT1704-A618, 2004.

[2] J. Diebold, *The Effects of Turbulence on the Measurement of Five-Hole Probes*. PhD thesis, 12 2016.

[3] R. Dominy and H. Hodson, "An Investigation into the Effects of Reynolds Number and Turbulence upon the Calibration of 5-Hole Cone Probes," *Symposium on Measuring Techniques in Transonic and Supersonic Flow in Cascades and Turbomachines*, no. MTT0988-A723, 1988.

[4] J. Coull, T. Dickens, H. Ng, and J. Serna, "Pneumatic-probe measurement errors caused by fluctuating flow angles," *AIAA Journal*, vol. 61, no. 7, pp. 2922–2931, 2023.

[5] M. de Guzman, C. Fletcher, and J. Hooper, "Computational Investigation of Cobra Probe Operation," *International Journal of Numerical Methods for Heat & Fluid Flow*, vol. 4, no. 5, pp. 425–445, 1994.

[6] S. Coldrick, P. Ivey, and R. Wells, "The Influence of Compressor Aerodynamics on Pressure Probes: Part 2 - Numerical Models," *Proceedings of the ASME Turbo Expo*, pp. 515–520, 2004.

[7] J. Aschenbruck, T. Hauptmann, and J. Seume, "Influence of a Multi-Hole Pressure Probe on the Flow Field in Axial-Turbines," *Proceedings of 11th European Conference on Turbomachinery Fluid Dynamics & Thermodynamics*, 2015.

[8] C. Sanders, M. Terstegen, M. Hölle, P. Jeschke, H. Schönenborn, and T. Fröbel, "Numerical Studies on the Intrusive Influence of a Five-Hole Pressure Probe in a High-Speed Axial Compressor," *Proceedings of the ASME Turbo Expo*, 2017.

[9] M. Passmann, S. aus der Wiesche, and F. Joos, "Numerical Calibration of 3D Printed Five-Hole Probes for the Transonic Flow Regime," *Proceedings of the ASME - JSME - KSME Joint Fluids Engineering Conference*, 2019.

[10] C. Schäffer, K. Speck, and V. Gümmer, "Numerical Calibration and Investigation of the Influence of Reynolds Number on Measurements With Five-Hole Probes in Compressible Flows," *Journal of Turbomachinery*, vol. 144, 2022.

[11] A. Torre, M. Patinio, G. Lopes, L. Simonassi, and S. Lavagnoli, "Vane–Probe Interactionsin Transonic Flows," *Journal of Turbomachinery*, vol. 145, 2023.

[12] K. A. Diáz, J. F. Oro, E. B. Marigorta, and R. B. Perotti, "A Numerical 3-D Model of a Trapezoidal Three-Hole Pneumatic Pressure Probe for Incompressible Flow," *Proceedings of the ASME Fluids Engineering Division Summer Conference*, no. MTT1704-A618, pp. 159–167, 2010.

[13] J. Taylor and W. Thompson, *An introduction to error analysis: the study of uncertainties in physical measurements*, vol. 2. Springer, 1982.

[14] M. Hölle, C. Bartsch, and P. Jeschke, "Evaluation of Measurement Uncertainties for Pneumatic Multihole Probes Using a Monte Carlo Method," *Journal of Engineering for Gas Turbines and Power*, vol. 139, p. 072605, 03 2017.

[15] Ansys, "Ansys Fluent Mosaic Technology Automatically Combines Disparate Meshes with Polyhedral Elements for Fast, Accurate Flow Resolution," *Ansys - White Paper*, November 2020.

[16] I. Celik, U. Ghia, P. Roache, and C. Freitas, "Procedure for Estimation and Reporting of Uncertainty Due to Discretization in CFD Applications," *Journal of Fluids Engineering*, vol. 130, p. 078001, 07 2008.

[17] F. Menter, R. Lechner, and A. Matyushenko, "Best Practice: Generalized k-omega Two-Equation Turbulence Model in Ansys CFD (GEKO)," *Ansys - Technical Report*, 2020.